Title

Controlled Assembly of Upconverting Nanoparticles for Low-Threshold Microlasers and Their Imaging in Scattering Media

Journal

ACS Nano, 14(2)

ISSN

1936-0851

Authors

Liu, Yawei

Teitelboim, Ayelet

Fernandez-Bravo, Angel

et al.

Publication Date

2020-02-25

DOI

10.1021/acsnano.9b06102

Peer reviewed

Controlled Assembly of Upconverting Nanoparticles for Low-Threshold Microlasers and Their Imaging in Scattering Media

Yawei Liu,[‡1,2] Ayelet Teitelboim,[‡1,] Angel Fernandez-Bravo,[1] Kaiyuan Yao,[3,4] M. Virginia P. Altoe,[1] Shaul Aloni,[1] Chunhua Zhang,[2] Bruce E. Cohen,[1] P. James Schuck,[3] and Emory M. Chan[1*]

The Molecular Foundry, Lawrence Berkeley National Laboratory, Berkeley, CA 94720, USA

[‡] These authors contributed equally to this work.

[*] To whom correspondence should be addressed. E-mail: EMChan@lbl.gov

[1]The Molecular Foundry, Lawrence Berkeley National Laboratory, Berkeley, CA 94720, USA

[2]School of Chemistry and Chemical Engineering, Harbin Institute of Technology, Harbin 150001, China

[3]Department of Mechanical Engineering, Columbia University, New York, NY 10027, USA

[4]Department of Mechanical Engineering, University of California, Berkeley, CA 94720, USA

ABSTRACT

Micron-sized lasers fabricated from upconverting nanoparticles (UCNP) coupled to whispering gallery mode (WGM) microresonators can exhibit continuous-wave Anti-Stokes lasing useful for tracking cells, environmental sensing, and coherent stimulation of biological activity. The integration of these microlasers into organisms and microelectronics requires even smaller diameters, however, which raises threshold pump powers beyond practical limits for biological applications. To meet the need for low lasing thresholds and high fidelity fabrication methods, we use correlative optical and electron microscopy to uncover the nanoparticle assembly process and structural factors that determine efficient upconverted lasing. We show that 5-μm microspheres with controlled submonolayer UCNP coatings exhibit, on average, 25-fold lower laser thresholds (1.7 ± 0.7 kW/cm^2) compared to the mean values of the lowest threshold UCNP lasers, and variability is reduced 30-fold. WGMs are observed in the upconversion spectra for TiO_2-coated microspheres as small as 3 μm, a size at which optical losses had previously prevented such observations. Finally, we demonstrate that the WGM signatures of these upconverting microlasers can be imaged and distinguished through tissue-mimicking phantoms. These advances will enable the fabrication of more efficient upconverting lasers for imaging, sensing, and actuation in optically complex environments.

KEYWORDS: anti-Stokes laser, self-assembly, nanoparticle, microlaser, upconversion

Micron-sized lasers[1–6] produce narrow-band, coherent light from cavities small enough to be embedded in biological samples, enabling cell tracking,[7] remote sensing,[8] and future optogenetic applications.[9] The microscopic dimensions of these lasers also facilitate their on-chip integration as optical interconnects, modulators, and beam-steering phased arrays.[10,11] Microlasers that can be pumped with near infrared (NIR) light can be implanted in optically heterogeneous media such as brain tissue, leveraging the significantly reduced scattering, absorption, photodamage, and background at NIR wavelengths.[12,13] Applications that require lasing at shorter wavelengths can still utilize NIR pumping through the use of upconverting microlasers that emit at higher energies than their NIR excitation.[14,15] Most upconverting lasers, however, have been fabricated from lanthanide-doped materials in the form of bulk crystals or fragile glass fibers, restricting the use of these lasers in microscale applications.[16]

Progress in whispering gallery mode (WGM) microresonators has led to the fabrication of more compact upconverting microlasers.[17–20] For example, advances in the colloidal synthesis of lanthanide-doped upconverting nanoparticles[21–27] (UCNPs) now enable the facile, solution-phase fabrication of upconverting WGM microlasers with diameters as small as 5 μm.[24,28–31] The coating of polystyrene (PS) microspheres with $NaYF_4$:Tm^{3+} energy looping nanoparticles[12] (ELNPs) as the gain material resulted in upconverted WGM lasers with mean power density thresholds as low as 40 kW/cm^2.[29] These ELNP-PS microresonators exhibited stable upconverted lasing at both 450 and 800 nm under hours of pumping at 1064 nm. The record low thresholds of these 5 μm microlasers enabled pumping with cw excitation at room temperature,[29] whereas most lasers using nanoparticle gain media must be pumped with short, intense pulses and/or at cryogenic temperatures to avoid thermal degradation.[32–34]

The practical application of these UCNP microlasers requires resonators with smaller diameters, lower lasing thresholds, and higher fabrication fidelity. Microlasers that can operate at lower pump powers induce less photodamage and are critical to remote applications in

scattering media, where the pump intensity is attenuated. More compact lasers would minimize physical perturbation to biological samples and increase spatial energy confinement in optoelectronic devices. Moreover, smaller resonators are desirable because they reduce mode volumes, resulting in higher free spectral range, faster stimulated and spontaneous emission rates, and lower pump power thresholds (which are proportional to mode volume).[35,36] Smaller resonator diameters increase cavity losses, however; for microspheres, reflection losses at curved surfaces increase approximately exponentially with decreasing cavity radius.[36] These losses decrease cavity quality factor and increase thresholds.[31,35] A final obstacle limiting the application of microsphere lasers with nanoparticle gain media is that they exhibit a broad distribution of lasing thresholds across resonators and across nanoparticle batches.[1,29] This lack of fidelity suggests that a more complete understanding of the nanoparticle deposition process – and of the structural factors that determine efficient lasing – is needed.

Here, we demonstrate the fabrication of upconverting microspheres with lower lasing thresholds and reduced variability by controlling the assembly of ELNP layers at the outer surfaces of WGM microresonators. We correlated microsphere morphology, as measured by scanning electron microscopy, with the lasing performance measured by optical microscopy. Statistical analysis of single-bead data allowed us to identify reproducible methods for obtaining high quality lasing at low thresholds and for increasing control over the coating process. We found that manipulating the nanoparticle surface charge prior to the coating process is instrumental in the assembly of smooth, uniform submonolayers of ELNPs on the surface of PS microspheres, resulting in reduced spontaneous emission background and 25-fold lower mean threshold power with a 30-fold narrower distribution across different cavities. These superior microcavity morphologies allowed us to image upconverting microlasers through scattering media, and to access upconverted WGM lasing in inherently more lossy and smaller, 3 μm cavities.

RESULTS AND DISCUSSION

Elucidating the relationship between morphology and lasing performance. We fabricated our upconverting microlasers (Figure 1) by coating PS microspheres with gain material consisting of Tm^{3+}-doped, $NaYF_4$ energy-looping nanoparticles ($NaY_{0.99}Tm_{0.01}F_4$, 15.8 nm diameter) passivated with 2.2 nm-thick $NaY_{0.8}Gd_{0.2}F_4$ shells (shown in Figure S1 and Figure S2). PS polymers form porous colloids that swell and shrink depending on solvent polarity, and they present hydrophobic surfaces amenable to van der Waals interactions with the hydrocarbon tails of oleic acid ligands on ELNPs. The PS microspheres (Figure S3) were swelled with a polar solvent mixture (8 *v/v*% chloroform in butanol) in the presence of the ELNPs to drive the hydrophobic nanoparticles to form a halo in the outer-most layer of the microspheres. The swelled microspheres were de-swelled in ethanol, trapping the ELNPs at the outer surface, then purified to remove excess nanoparticles (see Methods and Supplemental Information).

In order to reveal the factors that influence the quality of lasing in our cavities, we used scanning electron microscopy and confocal upconversion microscopy to correlate the morphology and surface coverage of each microcavity with its lasing performance. Microlasers prepared with our previously reported process[29] exhibit a broad distribution of lasing thresholds and a correspondingly large distribution of coating quality (Figure S4). Single cavity correlation experiments revealed that resonators with high surface roughness and large ELNP aggregates often produced only spontaneous emission (Figure S4a). Conversely, microresonators coated with fewer layers of ELNPs exhibited lower surface roughness that was linked to sharp WGM resonances, reduced spontaneous emission background, and lasing behavior (Figure S4b-d).

Fabricating cavities with submonolayer ELNP coatings. The above results suggest that cavities coated with a single layer of ELNPs might exhibit the highest lasing performance (*e.g.*, high WGM intensity and low spontaneous emission), but isolating process conditions that

promote the self-assembly of single layers is challenging due to the large bead-to-bead variation in coating morphology. Noting that large changes in surface roughness and bead-to-bead reproducibility occurred when switching batches of ELNPs, we hypothesized that the ELNP deposition process was sensitive to variations in the small excess of oleic acid ligand used to stabilize the ELNPs in suspension, which is variable and difficult to quantify during post-synthesis nanoparticle purification.

To test this hypothesis, we incorporated additional oleic acid into the fabrication of our ELNP-PS microresonators, which is initiated by mixing two components: (1) a dispersion of ELNPs in hexane, and (2) a suspension of PS microspheres in an 8% (*v*/*v*) chloroform/*n*-butanol mixture. Specifically, we added variable amounts of oleic acid to the ELNP/hexane solutions (Component 1) before they were mixed with the chloroform/*n*-butanol suspension (see SI Methods). (Component 2). For consistency, we used the same batch of purified ELNPs for this experimental series. When no additional OA was added, the resulting cavities were coated with thick layers of ELNPs with high surface roughness (Figure 2a) and only a small fraction of these microresonators exhibited WGMs (Figure S5). As OA was added (1% and 5% *v*/*v* in Component 1), we observed thinner, more uniform ELNP coatings, along with the emergence of WGMs above the spontaneous emission spectra (Figure 2bc, Figure S6, Figure S7). Smooth, single-layer coatings of ELNPs were achieved at the highest OA concentration (*ca.* 10% OA in Component 1) as shown in Figure 2d and Figure S8). SEM images of these coatings appear to exhibit submonolayers of loosely packed ELNPs that incorporate occasional voids and isolated regions with multiple layers or aggregates that are two or three ELNPs in thickness (Figure S9). These imperfections are reasonable given the expected roughness of PS surface, which is known to be mobile and porous when solvated.

To further characterize the submonolayer arrangement of ELNPs at the surface of the microsphere, we used transmission electron microscopy to image cross-sections (50 and 100 nm in thickness) of the ELNP-PS microcavities prepared by microtome sectioning of

microspheres embedded in epoxy. Micrographs of the cross-sections, imaged with energy filtering contrast (Figure 2ef), show ELNPs arranged in a thin submonolayer coating on the rough PS surface (additional cross-sections shown in Figure S10). These images are consistent with our interpretation of SEM micrographs and validate our assumption that a high OA concentration during assembly results in a loosely packed submonolayer coating. The ELNP submonolayer follows the contours of the rough PS surface (Figure 2g), in contrast to the thick, aggregated coating observed in cross sections of microspheres prepared with low OA concentration (Figure S11).

To test the reproducibility of this microlaser assembly, we randomly selected 15 microspheres for analysis by SEM (Figure S8). The smooth, submonolayer morphology observed with the highest OA (10% OA in ELNP/hexane stock solution) is reproducible across the samples, in contrast to the wide variability when OA is not added. Adding 10% OA, we observed a significant improvement in the corresponding lasing spectrum for each microresonator, as apparent in the narrow and intense WGMs and the diminished spontaneous emission background. To quantify the lasing performance as a function of the sample processing, we calculated the quality factor ($Q=\frac{\lambda_{mode}}{\Delta\lambda_{mode}}$) for the WGMs observed for each resonator. Here, λ_{mode} is the resonance wavelength of a WGM and $\Delta\lambda_{mode}$ is its spectral full width at half maximum. As shown in Figure S12, an increasing trend can be seen for Q as a function of increasing OA concentration in the ELNP solution. More significantly, the spread of Q over different cavities narrows with increasing OA concentration, highlighting the improvement in the reproducibility of the cavity morphology and optical performance.[37–39]

To better capture both the WGM line narrowing and the contrast between the mode and the spontaneous emission background, we defined a second figure of merit that we refer to as the "mode performance" factor, $MP=\frac{I_{mode}}{I_{SP}\cdot\Delta\lambda_{mode}}$. Here, I_{sp} is the intensity of the spontaneous emission center peak, and I_{mode} is the mode peak intensity. The ratio, $I_{mode}/I_{SP,}$ provides a

measurement of the contrast between the stimulated emission over spontaneous emission. $\Delta\lambda_{mode}$ incorporates the quality of the mode. *MP* reaches high values only when the WGMs display sharper peaks and higher contrast to the spontaneous emission, meaning more energy is funneled and stimulated into the lasing WGM.

Using this *MP* parameter to quantify the performance of different cavities, we observed that *MP* increases monotonically with OA concentration (Figure 3a). Notably, the distribution of *MP* values narrows substantially for the cavities processed with the highest OA percentage, with 80% of the cavities in the batch characterized by a high "*mode performance"* score (defined as $MP > 0.5$). Thus, the lasing performance for the different samples summarized in Figure 3a shows a clear correlation between high quality lasing and the uniform assembly of ELNP single layers on PS beads.

ELNP surface charge drives assembly of submonolayers. To understand why oleic acid has such a strong influence on ELNP deposition, we used ζ-potential measurements to measure the charge of the ELNPs as a function of OA concentration in the deposition solution (92 *v/v*% *n*-butanol and 8 *v/v*% chloroform). The ζ-potential of the ELNPs becomes more positive as more OA is added (Figure 3b), indicating that the excess oleic acid confers positive charge to the ELNP surfaces. This positive charge is consistent with measurements by Shevchenko *et al*,[40] who found that conferring positive charge to nanoparticles with added oleic acid produced more consistent interparticle forces that facilitated the ordered assembly of nanoparticle superlattices. The positive charge could originate from the protonation of oleate ligands coordinated to metal cations at the nanoparticle surfaces.[40] Such protonation could be driven by the ready dissociation of the added oleic acid (pK_a *ca.* 5.0 in water[41,42]) and its large excess relative to surface-bound oleate species. We infer that the excess oleic acid saturates the nanoparticle surfaces, resulting in both steric and Coulombic repulsion that prevents aggregation and facilitates the assembly of individual nanoparticles (rather than microscopic aggregates) on the

PS surface (Figure 3c and d).[43] Further driving the conformal assembly is the fact that the surfaces of untreated PS microspheres display negatively charged sulfonate groups which may attract the oppositely charged ELNPs[44] or displace ELNP oleates to interact with cationic ad-atoms on the nanoparticle surface.[21] This attraction is self-limiting, since the electrostatic repulsion between particles discourages the growth of additional ELNP layers. Thus, high concentrations of OA control the surface charge and increase the uniformity of the charge of the ELNPs, facilitating the finely controlled assembly of ultra-thin ELNP submonolayers.

High-fidelity, low-threshold lasing from 5-µm, submonolayer-coated cavities. Inspired by our ability to assemble single layers of ELNPs onto PS microspheres, we sought to characterize the lasing properties of these microcavities. Figure 4 shows the superior lasing properties achieved for the submonolayer coated microspheres with high fidelity and reproducibility. The power dependent properties of the UC lasing cavities, as a function of the 1064 nm cw pump power (P_{ex}), are shown in Figure 4a-c for the two main WGM peaks centered at 798 and 807 nm. The emission intensity (I_{em}), calculated by integrating each WGM peak around its FWHM boundaries (shaded region in Figure 4d), exhibits a sharply increasing slope as the P_{ex} increases, characteristic of a lasing threshold. The power dependence curves were fit to a power law: $I_{em}=a\cdot P_{ex}^{S_p}$, in three regions of the curves (pre-lasing, lasing and saturation). The pre-lasing quadratic dependence (S_p = 2) expected for a multi-photon upconversion process increases to higher nonlinear order (S_p = 4.9) after the onset of lasing and gain buildup, representing the rise of stimulated emission. The high power dependence after the threshold is attractive for lasing applications, where a rapid increase in the emission output following a small increase in pump input is desirable. The lasing threshold (P_{th}), marked with a magenta star in Figure 4a and b, was assigned as the intersection of the pre-lasing and lasing line fits, showing an agreement between the lasing threshold onset and the narrowing of the WGM FWHM spectral linewidth.

High quality upconverted lasing was achieved for both competing modes (Figure 4a and b). This is characterized by the low lasing thresholds of 0.7 and 0.6 kW/cm^2 and narrow FWHM of 0.8 and 1 nm, corresponding to Q factors of $1 \cdot 10^3$ and $0.8 \cdot 10^3$, respectively. Furthermore, the emission spectra of the WGM lasing microsphere around the 800 nm Tm^{3+} peak show good agreement with calculated WGM resonance asymptotic solutions (Figure 4c and d; see Supplemental Information for mathematical description). To verify that these lasing modes were consistent with those expected for the size and refractive index of the cavities, we simulated their WGM spectral resonances using Finite Difference Time Domain (FDTD) modeling. For the case of 5 μm spheres coated with 20 nm $NaYF_4$, we observed good agreement between measured and simulated resonances (Figure S13). Furthermore, the simulated field distribution is consistent with the experimental far field image of a lasing microsphere (Figure S14).

The low experimental thresholds for submonolayer-coated microresonators were reproducible across 20 randomly selected microresonators. As shown in the histogram in Figure 4f, P_{th} values range from 0.5 to 3.5 kW/cm^2 with 65% of the beads focused between 1 to 2 kW/cm^2, further validating our ability to make high quality microlasers with high fidelity. To further confirm the homogeneity of our ELNP coating, we analyzed the threshold as a function of excitation pump position (Figure S15-S17). The threshold does not vary significantly with the pump coupling position, as expected of high quality homogeneous cavities.

Highlighting the improvement in optical performance afforded by control over cavity morphology, the mean lasing threshold of 1.7 ± 0.7 kW/cm^2 for submonolayer-coated ELNP-PS cavities are over 25-fold lower than the lowest reported average thresholds for upconverting nanoparticle lasers (44 ± 23 kW/cm^2), and the variability, calculated as one standard deviation from the mean, is 30-fold narrower. From these results it is apparent that a homogeneous coating of nanoparticle gain medium, especially a single layer of ELNPs, results in consistently high lasing quality.

Optical origins of improved lasing performance. We postulated that the improved lasing performance from these microcavities could be due to the enhanced coupling of the submonolayers to the WGMs, or due to the reduction in the cavity losses arising from surface imperfections.[37–39] Reducing the thickness of the $NaYF_4$ coating could also influence the refractive index and thus optical quality of the cavity, but FDTD simulations show that varying the $NaYF_4$ coating thickness from 20 to 100 nm has minimal effect on cavity *Q*-factors (Figure S18 and Table S2).

For the improvement in coupling to be significant, the coupling of additional ELNP layers would need to be weaker. Since the electric field distribution of the WGMs extends *ca.* 100 nm outside the surface of the PS microsphere at the 800 nm resonance wavelength (λ),[45] this explanation is only valid for thick, disordered coatings (as in Figure 2a) with surface roughness greater than 100 nm. In this case, stimulated emission would decrease in favor of spontaneous emission, and lasing thresholds would increase. However, the reduced coupling of multilayered coatings cannot be the sole explanation for the improved performance of these cavities since we observed low mode performance even for coatings thinner than 100 nm.

Hence, we turn our focus to our second hypothesis: that the uniform ELNP submonolayers reduce cavity losses caused by surface imperfections, such as variations in the coating thickness or inhomogeneity in the refractive index. Surface roughness plays a critical role in the quality of WGM cavities, and numerous studies outline the role of cavity roughness in device design and fabrication.[37–39,46,47] Simulations by Rahachou and Zozoulenko using a scattering matrix approach have demonstrated that surface roughness on the order of $\lambda/5$ can completely suppress the lasing of the disk resonators and variations as small as $\lambda/30$ can drastically degrade high-*Q* WGM resonances.[37,46] This surface roughness reduces the local radius of the internal cavity interface, increasing transmission of light through the interface and out of the cavity, thereby decreasing *Q*.

To test whether additional layers of ELNPs on the cavities induce losses that sacrifice the quality of WGMs, we attempted to induce scattering by depositing large (250 nm wide and 120 nm thick), hexagonal ELNPs (Figure S19) around submonolayer-coated ELNP-PS cavities. When surrounded by the large ELNPs, the strong WGMs previously observed for the same submonolayer-coated cavities disappeared, and only spontaneous emission was observed (Figure S20 and Figure S21). This complete quenching of WGMs occurred even for cavities surrounded by a small number of additional ELNPs at the base of the microspheres (Figure S20b and c), and even though the cavities were excited on the areas of the cavities coated with only single layers of ELNPs. These observations support our hypothesis that ELNP layers beyond the thin initial layer increase lasing thresholds primarily through surface imperfections-induced losses, illustrating the crucial role of the submonolayer coating in facilitating high quality WGM lasing for 20 nm ELNPs. Furthermore, our difficulty in conformally depositing secondary layers on oleic acid-treated ELNP monolayers is consistent with our deposition model since the additional ELNPs would be electrostatically repelled by the positively charged monolayers on the surface of the microcavities.

To test our hypothesis further, we assembled the hexagonal ELNPs directly onto the surface of PS microspheres using our improved fabrication method (Figure 5; additional examples in Figure S22). By tuning the concentration of the ELNPs, we produced coatings (Figure 5a, d) ranging from submonolayers of the nanoplates to close packed layers of one to two layers in thickness. Compared to the microspheres coated with 20 nm ELNPs, the cavities coated with submonolayers of the larger ELNPs exhibited lasing spectra with broader mode resonances (Figure 5b) and correspondingly lower Q of *ca.* 275. These peaks were further broadened when packing one more monolayers of ELNPs onto the PS microspheres (Figure. 5e, S22c, d), corresponding in a reduction of Q to 196 and an increase in the laser threshold. The reduced lasing performance of these large ELNPs – in both submonolayers and dense multi-layered coatings – mimics that of thick, irregular coatings of the smaller, 20 nm ELNPs,

even though the larger nanoplates should be disproportionately brighter and therefore have higher gain than the smaller ELNPs. This observation further supports our hypothesis that thick coatings and rougher surfaces increase the cavity losses, reduce stimulated emission gain, and lower the quality of WGMs.[37–39]

The fact that both large, ELNP plates and small spheres assemble onto microresonators highlights the generality of our deposition method. The domains of close-packed nanoplates in Figure 5 suggest that future optimization of their deposition may provide a route to the self-assembly of complete shells of two-dimensional nanoplate superlattices with uniform monolayer thickness that will enhance lasing.

Imaging lasers in scattering media. To illustrate the general applicability of our low-threshold UCNP lasers for biological applications such as tracking analyses in tissue, we imaged the microlasers through phantoms that simulate the scattering of biological tissue (instrumental setup shown in Figure 6a). Submonolayer-coated, 5 μm ELNP microlasers exhibited sharp WGMs and lasing even when pumped through 1 mm thick phantoms synthesized with 1% w/v agarose and 0.25% w/v intralipid (Figure 6bd). The overall intensity of the microlaser shown in Figure 6b was reduced *ca.* 8-fold (relative to imaging without the phantom) due to the phantom's scattering of the excitation and emitted light (More results showed in Figure S23). The fact that the submonolayer-coated microlasers could still achieve cw lasing even with such scattering highlights the significance of their dramatically lower thresholds relative to previously reported UCNP microlasers. Hyperspectral imaging of the lasers (Figure 6cd) also confirmed that small variations in the size of the PS microspheres alter their spectral features, shifting the intensity and position of their WGMs. These spectral fingerprints (Figure 6d and S24) can be used to distinguish individual lasers in an ensemble. In the image in Figure 6c, the color of a given pixel is determined from the amplitudes extracted from fitting the spectrum acquired at that point to the weighted combination of the average spectrum of each microsphere. While microspheres 1 and 5 in Figure 6c cannot be distinguished due to the similarity of their

spectra, Microspheres 2-4 in Figure 6c can be spectrally resolved without interference, highlighting the ability of these microlasers to act as barcode-type labels in highly scattering media. Similar results were obtained using the amplitudes of Lorentzian fits to the WGMs, as shown in Figure S25.

Reducing cavity dimensions to 3 μm. Encouraged by the ability to fabricate submonolayer-coated microspheres that exhibit high quality lasing even in scattering media, we hypothesized that such performance would allow us to observe lasing in smaller PS cavities with inherently higher losses. To date, upconverting microlasers have not been demonstrated in microspheres less than 5 μm in diameter. Unlike previous attempts, coating PS microspheres with a single layer of ELNPs enabled us to observe whispering gallery resonant features for 3 μm resonators (Figure 7a-c and S13b), as evident in a survey of 10 representative microcavities (Figure 7e). The WGM resonances in Figure 7c and Figure S13 fit well with values calculated from Finite Difference Time Domain (FDTD) simulations (orange symbols) and from asymptotic solutions (the transverse electric and magnetic mode field distribution $|E|^2$ of these simulations are shown in Figure 7d and Figure S26). The threshold of the 3 μm cavity was 1.1 kW/cm^2, comparable with the thresholds of the 5 μm cavities. The smaller cavity had broader FWHM (5 nm), corresponding to a 10-fold lower Q factor ($1.5 \cdot 10^2$) compared to the 5 μm cavities.

Although the width of the WGMs observed for the 3 μm cavities are relatively broad, the fact that some significant resonant amplification and coupling to the cavity WGMs could be observed indicates that we were able to improve the cavity morphology to increase stimulated emission gain. From the FDTD simulation (Figure 7c, orange line), it is apparent that the resonant peaks can be matched to the features measured for the 3 μm cavities. The FDTD results illustrate the inherent high cavity losses and low Q, evident in the broad width of the resonant peaks and consistent with our measurements. To counteract the lower Q of the 3 μm cavities, we used atomic layer deposition (ALD) to overcoat the smaller ELNP-PS microresonators with 20 nm of high-index TiO_2 (Figure 7f). With a refractive index around 2.4

(compared to 1.586 for PS), TiO_2 increases the refractive index contrast between the cavity and the surrounding air, improving light confinement. Furthermore, the conformal ALD coating substantially reduced the remaining surface roughness of the ELNP-PS microcavities (Figure 7). The ALD TiO_2 coating resulted in an improved *Q* factor relative to the uncoated microspheres (Figure 7), as evident in sharper WGMs displayed by the 10 representative microspheres in Figures 7g (see also Figure S13c). The dominant WGM mode of the microsphere depicted in Figure 7j exhibited a FWHM of 3.2 nm, resulting in a >50% higher *Q* (*ca.* 250) relative to the uncoated 3 μm cavities. The threshold of 1.4 kW/cm^2 was comparable to that of the 3 μm microsphere lacking the TiO_2 coating. The WGM spectral resonances were simulated using FDTD for the case of a 3 μm PS sphere with a 20 nm $NaYF_4$ coating and an additional 20 nm TiO_2 coating. The simulated spectrum in Figure 7j shows good agreement between measured and simulated field enhanced resonances (see also Figure S13 for log plot).

These results indicate that with TiO_2 encapsulation, more light is retained in the microsphere cavity, and more energy is coupled to the lasing mode. Reducing the cavity's size also leads to fewer competing WGM modes, which is instrumental in achieving the single mode lasing apparent in the measured and calculated spectra in Figure 7j. Reducing the resonator diameter improves their utility for applications such as biological imaging, since their smaller volumes (14 μm^3) should promote their uptake into cells (*ca.* 100 μm^3 for red blood cells) and transmission through vasculature (typically 5 μm for capillaries).[7]

CONCLUSION

We have demonstrated the clear relationship between the nanoparticle deposition method, physical morphology, and lasing quality for upconverting nanoparticle microresonators. The ability to control the assembly of ELNP layers on the surface of PS microspheres was shown to reduce cavity losses and improve coupling to WGM resonances. This assembly was finely tuned by manipulating the surface charge of the nanoparticles to

promote coating of uniform submonolayer of particles. Microresonators fabricated using this method exhibited 25-fold lower average lasing threshold distributed over a 30-fold narrower power range. Taking advantage of this improved lasing performance, we were able to image the microlasers through scattering media and detect WGM resonance features for 3 μm diameter PS spheres. The insight into the assembly of nanoparticles on microcavities, including the importance of surfactant composition, surface roughness, and nanoparticle size effects, will be valuable for improving the performance and consistency of nanocrystal-coated lasers based on microspheres,[1] microfabricated toroids,[3] freely suspended microdisks,[4] and plasmonic nanocavities.[48]

Compared to coatings that embed nanoparticles in polymers or sol-gels,[1,6] the direct deposition of ELNP submonolayers onto microcavities offers advantages such as a larger number of nanoparticles actively coupled to WGMs and higher loading efficiencies. Our method does not require ligand exchange, and it scalably produces microresonators freely suspended in solution, which is required for biological applications. Decreasing the variability, thresholds, and diameters of cw upconverted microlasers will facilitate their adoption in biological applications towards imaging, sensing, and optogenetics, as well as optoelectronics applications such as 3D mapping, telecommunications, and solid-state lighting. These microlasers can be controllably coated with any type of nanoparticle, as shown by our ability to observe lasing from ELNPs ranging in size from 20 to 250 nm. The emission wavelengths and lasing performance can be tuned for applications by varying dopant compositions or by co-depositing mixed layers of nanocrystals with different compositions; we observed lasing at red (660 nm), green (540 nm) and purple (405 nm) wavelengths from microspheres coated with UCNPs codoped with 20% Yb^{3+} and 2% Er^{3+} (Figure S27). This combination of robust assembly and facile engineering of the complex energy transfer networks[49] within doped nanoparticles will enable the generation of expansive libraries of UV, visible, and NIR

microlasers catered to any application in which small size, low input power, and concentrated coherent light are needed.

METHODS

Nanocrystal synthesis. 15.8 nm diameter $NaY_{0.99}Tm_{0.01}F_4$ ELNP cores with 2.2 nm-thick $NaY_{0.8}Gd_{0.2}F_4$ shells were synthesized using previously reported procedures.[12,29] Large, 250 nm wide, 120 nm thick $NaY_{0.99}Tm_{0.01}F_4$ hexagonal plates were synthesized from rare earth trifluoroacetate precursors in oleic acid and octadecene using modifications of a previously reported robotic nanocrystal workflow.[50] Detailed synthesis and characterization procedures are given in the Supporting Information.

Microlaser fabrication. ELNP-PS microresonators were fabricated by adding 5 μL of a 10 wt% aqueous suspension of 3 or 5 μm-diameter uncrosslinked polystyrene microspheres (Sigma-Aldrich #79166, #79633) to a mixture of 137 μL butanol and 12 μL chloroform. The absence of crosslinking in the PS is a crucial detail in this specific fabrication procedure since crosslinking modifies the swelling and alters the infiltration of the nanoparticles into the polymer. Purified, as-synthesized ELNPs (20 mg) were dissolved in 100 μL hexane in a 4 mL vial. Optionally, different amounts of oleic acid (1, 5 and 10 μL) were added to the above ELNP/hexane solution and sonicated for 10 min. The resulting ELNP/hexane stock solutions were approximately 1, 5, and 10 *v*/*v*% OA, respectively, as they are referred to in the main text. 7.5 μL of the 0.2 g/mL ELNP stock solution in *n*-hexane with 0, 1, 5, or 10 *v*/*v*% oleic acid was added to the PS suspension, vortexed and sonicated for 5 s each, and then incubated for 4 h at room temperature without agitation. The ELNP-PS cavities were isolated by centrifugation (4000 rcf, 4 min) and washed with solvent four times, alternating between ethanol (the first wash) and *n*-hexane. For each ethanol wash step, 1000 μL ethanol was added to the microspheres, followed by vortexing and sonication for 5 s each, then centrifugation (4000 rcf,

4 min). For each hexane wash step, 1000 μL of *n*-hexane was added, followed by vortexing for 5 s and sonication for 1 min, and centrifugation (1100 rcf, 2 min).

Atomic layer deposition. ELNP-PS microresonators were drop cast from their ethanol suspension onto a silicon substrate and stored in a vacuum desiccator overnight. Then the silicon substrate was transferred into an Oxford FlexAl-Plasma Enhanced Atomic Layer Deposition (ALD) chamber. 20 nm of high index TiO_2 was deposited from tetrakis(dimethylamido)titanium precursor by performing 216 cycles at 40 °C.

Correlative microscopy. ELNP-PS microresonators were drop cast from an ethanol suspension onto a marked silicon substrate and dried in air. The emission spectra of single microspheres were obtained using a Horiba LabRam Aramis confocal microscope using a 100x NA 0.9 air Mplan N objective (Olympus), a 300 grooves/mm grating, and a 1064 nm continuous-wave excitation laser (Laser Quantum). The 1064 nm laser power density for correlative measurements was 10^6 W/cm^2 unless otherwise specified. The lasing performance of the single microspheres was correlated with its morphology and surface coverage, characterized using a Zeiss Ultra 55 field emission SEM. Markings on the silicon were used to find the same microspheres in both microscopes.

Confocal microscopy. ELNP-PS microresonators suspended in ethanol solution were drop cast onto #1 glass coverslips. Laser scanning confocal imaging was performed in ambient conditions using a custom-built confocal inverted microscope. The sample was excited using a 1064 nm continuous-wave laser excitation source (CrystaLaser CL1064-2W5) transmitted through a 900 long pass filter, a 1064 nm short-pass dichroic mirror (Di02-R1064, Semrock), and tightly focused using an oil-immersed objective (100x 1.4NA oil Plan Apo VC, Nikon). The emission was collected by the same objective, spectrally filtered using a 980 short pass filter (FF01-980/SP, Semrock), and imaged onto a spectrometer (Acton SpectraPro SP-2300i, Princeton instruments, coupled to a liquid nitrogen cooled Princeton instruments CCD), using a grating of 600 grooves/mm blazed at 750 nm to obtain the spectra. To control the excitation

laser power, a continuously variable, reflective neutral density filter wheel (Thorlabs) was inserted in the laser beam path. Excitation power was continuously monitored using a Thorlabs power meter.

Imaging through phantoms. Hyperspectral images were acquired in the confocal microscope using a 60x NA 0.7 long working distance Plan Fluor objective (Nikon). Polystyrene microspheres coated with ELNPs were suspended in ethanol solution and drop cast onto a silicon chip. Silicon wafers and glass slides were used as spacers to maintain a gap between the microspheres and the cover slip to allow the phantom to be inserted. A 1 mm thick phantom gel, prepared from 1% w/v agarose and 0.25% w/v Intralipid in water, was supported by a cover slide and placed on the spacers so that the phantom could be removed without moving other parts of the setup. This allowed the acquisition of images and emission spectra for a selected microsphere with and without the presence of the phantom.

Mode performance. The MP value was calculated by fitting the lasing emission spectrum using multiple Lorentzians centered at the different spectral peaks. The initial spectral peak centers were detected automatically, assigning narrow Lorentzian spectral linewidth for each detected WGM and a relatively wide Lorentzian for the spontaneous emission distribution). For calculating the MP factor's intensity ratio (I_{sp}/I_{mode}), the amplitudes of the Lorentzian fits were used. A similar method was used to calculate the lasing FWHM.

Simulations. Two different methods to calculate the WGM spectral resonance and field distribution were used. In the first method, we calculate the WGM center wavelength resonances $\lambda_{r,m,l}$ for the different radial (r) and angular (m) mode order integers, azimuthal peak number (l-m+1), and for both transverse magnetic (TM) and transverse electric (TE) modes, using the asymptotic approximation by Lam *et al*. In the second method, numerical simulations were made using Lumerical finite difference time domain (FDTD) software. It was used to simulated the resonance spectrum (electric field enhancement) of the dielectric microsphere

cavity and the electric field distribution within the sphere. PS beads (n_{PS}=1.586) were simulated on top of a glass substrate with 20 nm $NaYF_4$ coating (n_{NaYF_4}=1.465), representing the glass coverslip and the ELNP coating, respectively. For the case of microsphere coating an additional coating of 20 nm coating of TiO_2 (n_{TiO_2}=2.4) was used to simulate the titanium oxide-coated 3 μm beads. Further details about the simulation methods are described in the SI.

ACKNOWLEDGEMENTS

Y.L. was supported by a China Scholarship Council fellowship. A.T. was supported by the Weizmann Institute of Science − National Postdoctoral Award Program for Advancing Women in Science. P.J.S. acknowledges support by the Global Research Laboratory (GRL) Program through the National Research Foundation of Korea (NRF) funded by the Ministry of Science and ICT (no. 2016911815). This work was performed at the Molecular Foundry and was supported by the Office of Science, Office of Basic Energy Sciences, of the U.S. Department of Energy under Contract No. DE-AC02-05CH11231.

AUTHOR INFORMATION

Corresponding Author

EMChan@lbl.gov

Author contributions

‡These authors contributed equally.

Notes

The authors declare no competing interests.

ASSOCIATED CONTENT

Supporting Information

The Supporting Information is available free of charge on the ACS Publications website at DOI: 10.1021/acsnano.XXXXX.

Experimental materials and methods; FDTD simulation methods and data; discussion of the OA content associated with as-synthesized ELNPs; and additional optical, TEM, SEM, and XRD characterization of microlasers (Figures S1-S28).

REFERENCES

(1) Snee, P. T.; Chan, Y.; Nocera, D. G.; Bawendi, M. G. Whispering-Gallery-Mode Lasing from a Semiconductor Nanocrystal/ Microsphere Resonator Composite. *Adv. Mater.* **2005**, *17*, 1131–1136.

(2) Miao, P.; Zhang, Z.; Sun, J.; Walasik, W.; Longhi, S.; Litchinitser, N. M.; Feng, L. Orbital Angular Momentum Microlaser. *Science* **2016**, *353*, 464–467.

(3) Hsu, H.-S.; Cai, C.; Armani, A. M. Ultra-Low-Threshold Er:Yb Sol-Gel Microlaser on Silicon. *Opt. Express* **2009**, *17*, 23265.

(4) Schubert, M.; Steude, A.; Liehm, P.; Kronenberg, N. M.; Karl, M.; Campbell, E. C.; Powis, S. J.; Gather, M. C. Lasing within Live Cells Containing Intracellular Optical Microresonators for Barcode-Type Cell Tagging and Tracking. *Nano Lett.* **2015**, *15*, 5647–5652.

(5) Wang, T.; Yu, H.; Siu, C. K.; Qiu, J.; Xu, X.; Yu, S. F. White-Light Whispering-Gallery-Mode Lasing from Lanthanide-Doped Upconversion $NaYF_4$ Hexagonal Microrods. *ACS Photonics* **2017**, *4*, 1539–1543.

(6) Xing, G.; Liao, Y.; Wu, X.; Chakrabortty, S.; Liu, X.; Yeow, E. K. L.; Chan, Y.; Sum, T. C. Ultralow-Threshold Two-Photon Pumped Amplified Spontaneous Emission and Lasing from Seeded CdSe/CdS Nanorod Heterostructures. *ACS Nano* **2012**, *6*, 10835–

10844.

(7) Fikouras, A. H.; Schubert, M.; Karl, M.; Kumar, J. D.; Powis, S. J.; Di Falco, A.; Gather, M. C. Non-Obstructive Intracellular Nanolasers. *Nat. Commun.* **2018**, *9*, 4817.

(8) Pirnat, G.; Humar, M.; Muševič, I. Remote and Autonomous Temperature Measurement Based on 3D Liquid Crystal Microlasers. *Opt. Express* **2018**, *26*, 22615.

(9) Chen, S.; Weitemier, A. Z.; Zeng, X.; He, L.; Wang, X.; Tao, Y.; Huang, A. J. Y.; Hashimotodani, Y.; Kano, M.; Iwasaki, H. Parajuli, L. K.; Okabe, S.; Teh, D. B.; All, A. H.; Tsutsui-Kimura I.; Tanaka, K. F.; Liu, X.; McHugh, T. J. Near-Infrared Deep Brain Stimulation *via* Upconversion Nanoparticle–Mediated Optogenetics. *Science* **2018**, *359*, 679–684.

(10) Hill, M. T.; Gather, M. C. Advances in Small Lasers. *Nat. Photonics* **2014**, *8*, 908–918.

(11) Slusher, R. E. Semiconductor Microlasers and Their Applications. *Opt. Photonics News* **1993**, *4* (2), 8-17.

(12) Levy, E. S.; Tajon, C. A.; Bischof, T. S.; Iafrati, J.; Fernandez-Bravo, A.; Garfield, D. J.; Chamanzar, M.; Maharbiz, M. M.; Sohal, V. S.; Schuck, P. J; Cohen, B. E.; Chan E. M. Energy-Looping Nanoparticles: Harnessing Excited-State Absorption for Deep-Tissue Imaging. *ACS Nano* **2016**, *10*, 8423–8433.

(13) Xu, S.; Cui, J.; Wang, L. Recent Developments of Low-Toxicity NIR II Quantum Dots for Sensing and Bioimaging. *TrAC, Trends Anal. Chem.* **2016**, *80*, 149–155.

(14) Length, W.; Macfarlane, R. M. Unconversion Lasers. *Opt. Photonics News* **1992**, 9–15.

(15) Scheps, R. Upconversion Laser Processes. *Prog. Quantum Electron.* **1996**, *20*, 271–358.

(16) Piehler, D.; Craven, D.; Kwong, N.; Zarem, H. Laser-Diode-Pumped Red and Green Upconversion Fibre Lasers. *Electron. Lett.* **1993**, *29*, 1857.

(17) He, L.; Özdemir, Ş. K.; Yang, L. Whispering Gallery Microcavity Lasers. *Laser Photonics Rev.* **2013**, *7*, 60–82.

(18) Von Klitzing, W.; Jahier, E.; Long, R.; Lissillour, F.; Lefèvre-Seguin, V.; Hare, J.; Raimond, J. M.; Haroche, S. Very Low Threshold Green Lasing in Microspheres by Up-Conversion of IR Photons. *J. Opt. B: Quantum Semiclassical Opt.* **2000**, *2*, 204–206.

(19) Wu, Q.; Ward, J. M.; Nic Chormaic, S. Ultralow Threshold Green Lasing and Optical Bistability in ZBNA (ZrF_4–BaF_2–NaF–AlF_3) Microspheres. *J. Appl. Phys.* **2010**, *107*, 033103.

(20) Lissillour, F.; Ait Ameur, K.; Dubreuil, N.; Stephan, G. M.; Poulain, M. Whispering-Gallery-Mode Nd-ZBLAN Microlasers at 1.05 Mm. In *Proc. SPIE*; Saad, M., Ed.; 1998; p 150.

(21) Liu, D.; Xu, X.; Du, Y.; Qin, X.; Zhang, Y.; Ma, C.; Wen, S.; Ren, W.; Goldys, E. M.; Piper, J. A.; Dou, S.; Liu, X.; Jin, D. Three-Dimensional Controlled Growth of Monodisperse Sub-50 Nm Heterogeneous Nanocrystals. *Nat. Commun.* **2016**, *7*, 1–8.

(22) Liu, Y.; Lu, Y.; Yang, X.; Zheng, X.; Wen, S.; Wang, F.; Vidal, X.; Zhao, J.; Liu, D.; Zhou, Z.; Ma, C.; Zhou, J.; Piper, J. A.; Xi, P. Jin, D. Amplified Stimulated Emission in Upconversion Nanoparticles for Super-Resolution Nanoscopy. *Nature* **2017**, *543*, 229–233.

(23) Pilch, A.; Würth, C.; Kaiser, M.; Wawrzyńczyk, D.; Kurnatowska, M.; Arabasz, S.; Prorok, K.; Samoć, M.; Strek, W.; Resch-Genger, U.; Bednarkiewicz, A. Shaping Luminescent Properties of Yb^{3+} and Ho^{3+} Co-Doped Upconverting Core–Shell β-$NaYF_4$ Nanoparticles by Dopant Distribution and Spacing. *Small* **2017**, *13*, 54–66.

(24) Chen, X.; Jin, L.; Kong, W.; Sun, T.; Zhang, W.; Liu, X.; Fan, J.; Yu, S. F.; Wang, F. Confining Energy Migration in Upconversion Nanoparticles towards Deep Ultraviolet Lasing. *Nat. Commun.* **2016**, *7*, 1–6.

(25) Chan, E. M. Combinatorial Approaches for Developing Upconverting Nanomaterials: High-Throughput Screening, Modeling, and Applications. *Chem. Soc. Rev.* **2015**, *44*,

1653–1679.

(26) Fischer, S.; Swabeck, J. K.; Alivisatos, A. P. Controlled Isotropic and Anisotropic Shell Growth in β-$NaLnF_4$ Nanocrystals Induced by Precursor Injection Rate. *J. Am. Chem. Soc.* **2017**, *139*, 12325–12332.

(27) Tian, B.; Fernandez-Bravo, A.; Najafiaghdam, H.; Torquato, N. A.; Altoe, M. V. P.; Teitelboim, A.; Tajon, C. A.; Tian, Y.; Borys, N. J.; Barnard, E. S.; Anwar, M.; Chan, E. M.; Schuck, P. J.; Cohen, B. E. Low Irradiance Multiphoton Imaging with Alloyed Lanthanide Nanocrystals. *Nat. Commun.* **2018**, *9*, 4–11.

(28) Zhu, H.; Chen, X.; Jin, L. M.; Wang, Q. J.; Wang, F.; Yu, S. F. Amplified Spontaneous Emission and Lasing from Lanthanide-Doped up-Conversion Nanocrystals. *ACS Nano* **2013**, *7*, 11420–11426.

(29) Fernandez-Bravo, A.; Yao, K.; Barnard, E. S.; Borys, N. J.; Levy, E. S.; Tian, B.; Tajon, C. A.; Moretti, L.; Altoe, M. V.; Aloni, S.; Beketayev, K.; Scotognella, F.; Cohen, B. E.; Chan, E. M.; Schuck, P. J. Continuous-Wave Upconverting Nanoparticle Microlasers. *Nat. Nanotechnol.* **2018**, *13*, 572–577.

(30) Bian, W.; Lin, Y.; Wang, T.; Yu, X.; Qiu, J.; Zhou, M.; Luo, H.; Yu, S. F.; Xu, X. Direct Identification of Surface Defects and Their Influence on the Optical Characteristics of Upconversion Nanoparticles. *ACS Nano* **2018**, *12*, 3623–3628.

(31) Jin, L.; Wu, Y.; Wang, Y.; Liu, S.; Zhang, Y.; Li, Z.; Chen, X.; Zhang, W.; Xiao, S.; Song, Q. Mass-Manufactural Lanthanide-Based Ultraviolet B Microlasers. *Adv. Mater.* **2018**, 1807079.

(32) Adachi, M. M.; Fan, F.; Sellan, D. P.; Hoogland, S.; Voznyy, O.; Houtepen, A. J.; Parrish, K. D.; Kanjanaboos, P.; Malen, J. A.; Sargent, E. H. Microsecond-Sustained Lasing from Colloidal Quantum Dot Solids. *Nat. Commun.* **2015**, *6*, 1–8.

(33) Fan, F.; Voznyy, O.; Sabatini, R. P.; Bicanic, K. T.; Adachi, M. M.; McBride, J. R.; Reid, K. R.; Park, Y. S.; Li, X.; Jain, A.; Quintero-Bermudez, R.;

Saravanapavanantham, M.; Liu, M.; Korkusinski, M.; Hawrylak, P.; Klimov, V. I.; Rosenthal, S. J.; Hoogland, S.; Sargent, E. H. Continuous-Wave Lasing in Colloidal Quantum Dot Solids Enabled by Facet-Selective Epitaxy. *Nature* **2017**, *544*, 75–79.

(34) Grim, J. Q.; Christodoulou, S.; Di Stasio, F.; Krahne, R.; Cingolani, R.; Manna, L.; Moreels, I. Continuous-Wave Biexciton Lasing at Room Temperature Using Solution-Processed Quantum Wells. *Nat. Nanotechnol.* **2014**, *9*, 891–895.

(35) Lee, H.; Chen, T.; Li, J.; Yang, K. Y.; Jeon, S.; Painter, O.; Vahala, K. J. Chemically Etched Ultrahigh-Q Wedge-Resonator on a Silicon Chip. *Nat. Photonics* **2012**, *6*, 369–373.

(36) Kippenberg, T. J. Nonlinear Optics in Ultra-High-Q Whispering-Gallery Optical Microcavities; California Institute of Technology: Pasadena, California, 2004; Vol. 2004.

(37) Rahachou, A. I.; Zozoulenko, I. V. Effects of Boundary Roughness on a *Q* Factor of Whispering-Gallery-Mode Lasing Microdisk Cavities. *J. Appl. Phys.* **2003**, *94*, 7929–7931.

(38) Coillet, A.; Cibiel, G.; Lin, G.; Larger, L.; Furfaro, L.; Jacquot, M.; Henriet, R.; Chembo, Y. K. Dependence of Quality Factor on Surface Roughness in Crystalline Whispering-Gallery Mode Resonators. *Opt. Lett.* **2018**, *43*, 495–498.

(39) Cho, S.; Koo, S.; Yoo, K.; Pickett, E. R.; Park, N.; Kamins, T. I.; Park, B.-G.; Harris, J. S. Surface Roughness Effect on Q-Factor of Ge Whispering Gallery Mode Microdisk Resonator. In *Advanced Photonics*: OSA Technical Digest (CD); Optical Society of America: Washington, D.C., 2011; JTuB17.

(40) Shevchenko, E. V.; Talapin, D. V.; Kotov, N. A.; O'Brien, S.; Murray, C. B. Structural Diversity in Binary Nanoparticle Superlattices. *Nature* **2006**, *439*, 55–59.

(41) Lu, H. D.; Rummaneethorn, P.; Ristroph, K. D.; Prud'Homme, R. K. Hydrophobic Ion Pairing of Peptide Antibiotics for Processing into Controlled Release Nanocarrier

Formulations. *Mol. Pharmaceutics* **2018**, *15*, 216–225.

(42) Riddick, J.A.; Bunger, W. B.; Sakano, T. K. *Organic Solvents*; *Techniques of Chemistry*, 4th Ed.; John Wiley and Sons: New York, 1985; Vol. II, p. 379.

(43) Kravchenko, V. S.; Potemkin, I. I. Self-Assembly of Rarely Polymer-Grafted Nanoparticles in Dilute Solutions and on a Surface: From Non-Spherical Vesicles to Graphene-like Sheets. *Polymer* **2018**, *142*, 23–32.

(44) Lu, Y.; McLellan, J.; Xia, Y. Synthesis and Crystallization of Hybrid Spherical Colloids Composed of Polystyrene Cores and Silica Shells. *Langmuir* **2004**, *20*, 3464–3470.

(45) Oraevsky, A. N. Whispering-Gallery Waves. *Quantum Electron.* **2002**, *32*, 377–400.

(46) Rahachou, A. I.; Zozoulenko, I. V. Q Factors and Resonant States of Whispering-Gallery-Mode Dielectric Microdisk Cavities for Lasing Applications; In *Proc. SPIE, Laser Resonators and Beam Control VIII*; Kudryashov, A. V., Paxton, A. H., Eds.; SPIE: Bellingham, WA 2005; Vol. 5708, pp 210-221.

(47) Little, B. E.; Chu, S. T. Estimating Surface-Roughness Loss and Output Coupling in Microdisk Resonators. *Opt. Lett.* **1996**, *21*, 1390.

(48) Fernandez-Bravo, A.; Wang, D.; Barnard, E. S.; Teitelboim, A.; Tajon, C.; Guan, J.; Schatz, G. C.; Cohen, B. E.; Chan, E. M.; Schuck, P. J.; Odom, T. W. Ultralow-Threshold, Continuous-Wave Upconverting Lasing from Subwavelength Plasmons. *Nat. Mater.* **2019**, *18*, 1172–1176.

(49) Teitelboim, A.; Tian, B.; Garfield, D.; Fernandez Bravo, A.; Gotlin, A.; Schuck, J.; Cohen, B. E.; Chan, E. M. Energy Transfer Networks Within Upconverting Nanoparticles Are Complex Systems With Collective, Robust, and History-Dependent Dynamics. *J. Phys. Chem. C* **2019**, *123*, 2678-2689.

(50) Chan, E. M.; Xu, C.; Mao, A. W.; Han, G.; Owen, J. S.; Cohen, B. E.; Milliron, D. J. Reproducible, High-Throughput Synthesis of Colloidal Nanocrystals for Optimization

in Multidimensional Parameter Space. *Nano Lett.* **2010**, *10*, 1874–1885.

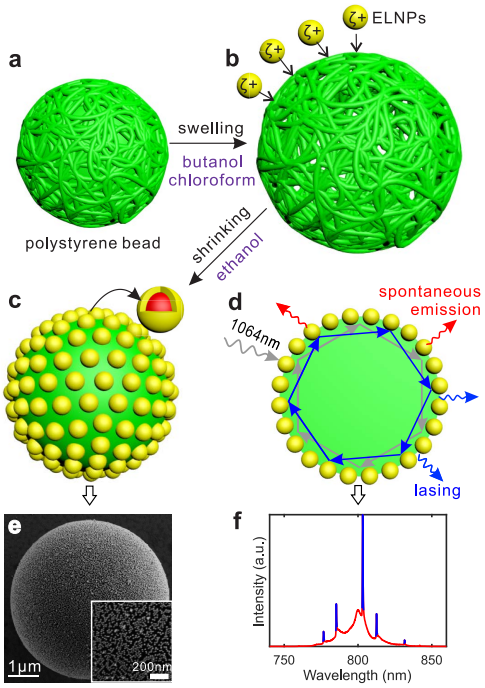

Figure 1. Upconverting microlasers based on energy looping nanoparticles (ELNPs) and polystyrene (PS) microspheres. (a-c) Fabrication of the ELNP-PS cavities: (a) PS cavity before surface treatment, (b) swelling PS bead in organic solvent mixture in the presence of ELNPs, and (c) shrinking of ELNP-coated cavity in polar solvent. (d) WGM resonances generated in an ELNP-PS cavity under 1064 nm pumping. (e) Scanning electron micrograph showing the morphology of an ELNP-PS cavity. The inset (right bottom) is the magnified view of the surface coated with nanoparticles. (f) Emission spectrum of an ELNP-PS microlaser, showing sharp whispering gallery modes (blue) and spontaneous emission (red).

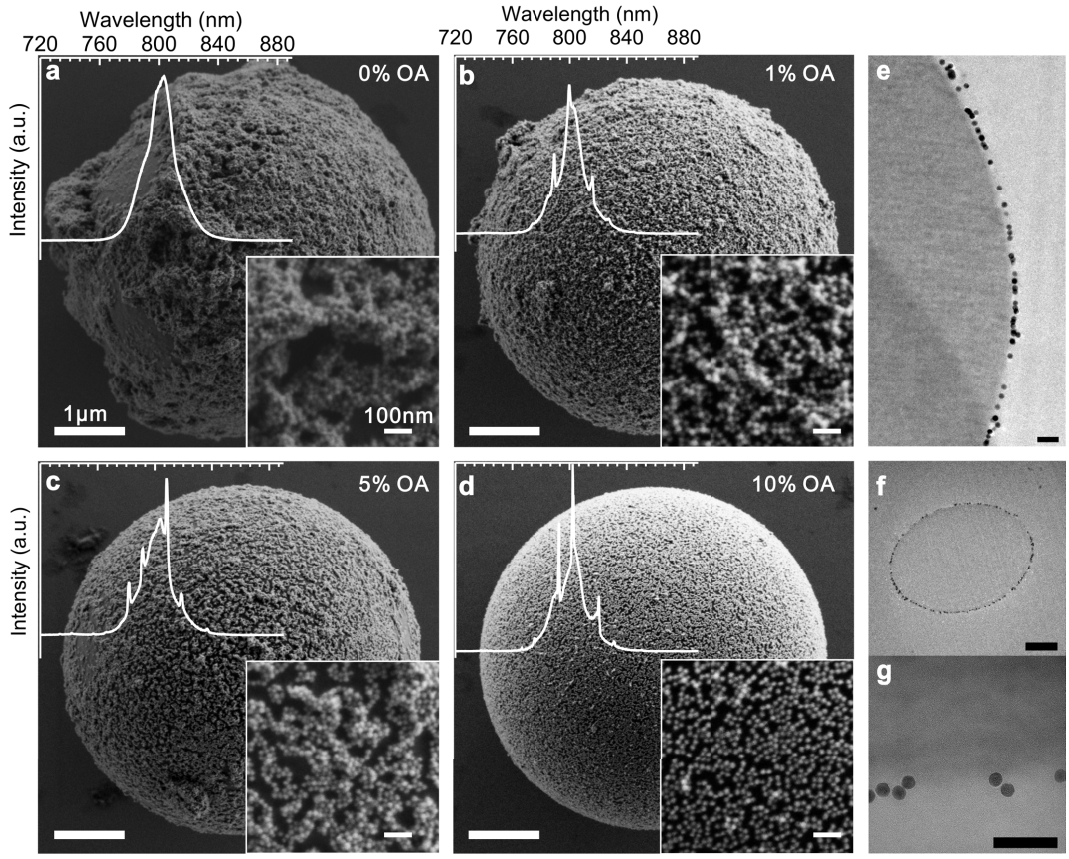

Figure 2. Effect of oleic acid on the surface coverage of ELNPs. (a-d) Scanning electron micrograph and emission spectrum (overlay) of ELNP-PS beads processed with ELNP suspended with (a) 0%, (b) 1%, (c) 5%, and (d) 10 v/v% oleic acid (OA). (e-f) TEM micrographs of epoxy embedded ELNP-PS microtome sectioning. Slices of 50 nm thickness are depicted using energy filter contrast to show the ELNPs (black) sub monolayer coating arrangement on surface of PS (grey). (e) PS surface submonolayer coating, scale bar 100 nm. (f) Full PS bead section and (g) magnified view of the PS/ELNP/epoxy interface showing the sub monolayer coating, with scale bars of 1 µm and 100 nm, respectively. The oval cross-section of the microsphere in (f) was induced by the strain of microtome sectioning.

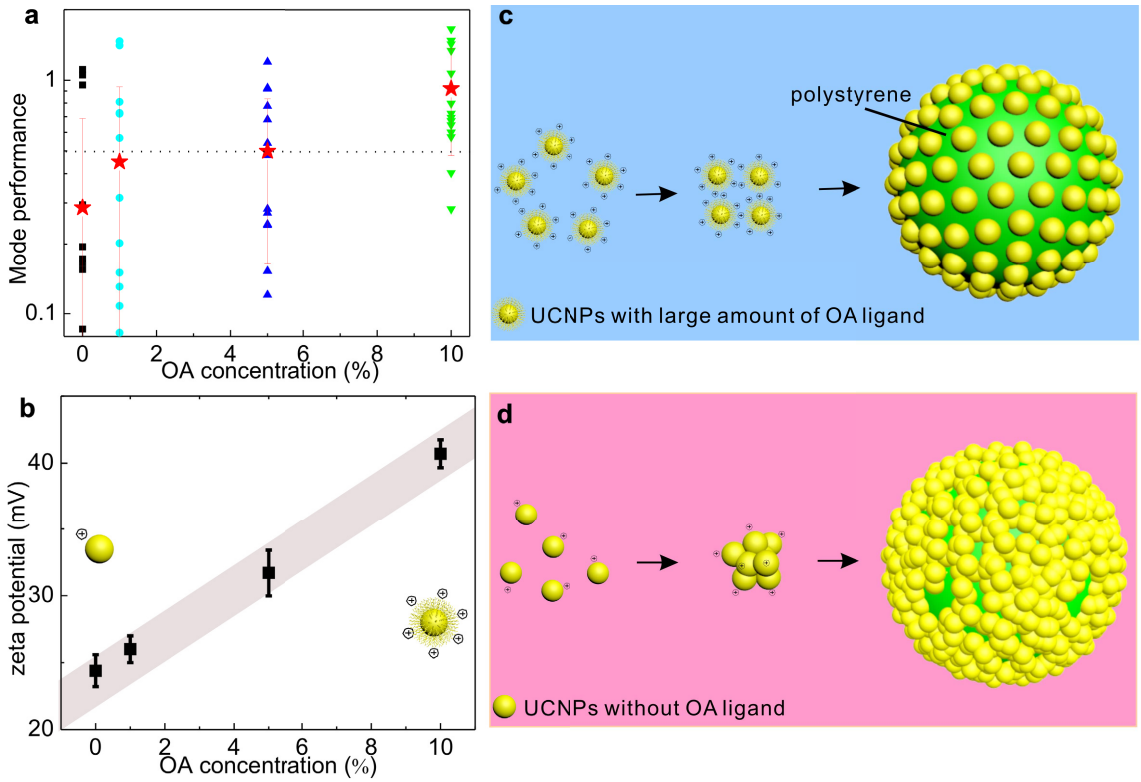

Figure 3. Effect of oleic acid on WGM quality and surface charge. (a) Mode performance factor for ELNP-PS cavities processed with increasing concentrations of OA. The mean and the standard deviation of the mode performance for the different OA concentrations are depicted by a red star and red bars respectively. (b) ζ potential of ELNPs as a function of OA ligand added to the processing mixture solution (92% butanol and 8% chloroform). (c-d) Schematic of the ELNP assembly on the surface of PS beads, showing the stabilizing effect of excess of OA ligands on the particles in solution, resulting in single layered coating (c). Alternatively, particles with no additional OA can aggregate, resulting in rough multilayered surface coverage (d).

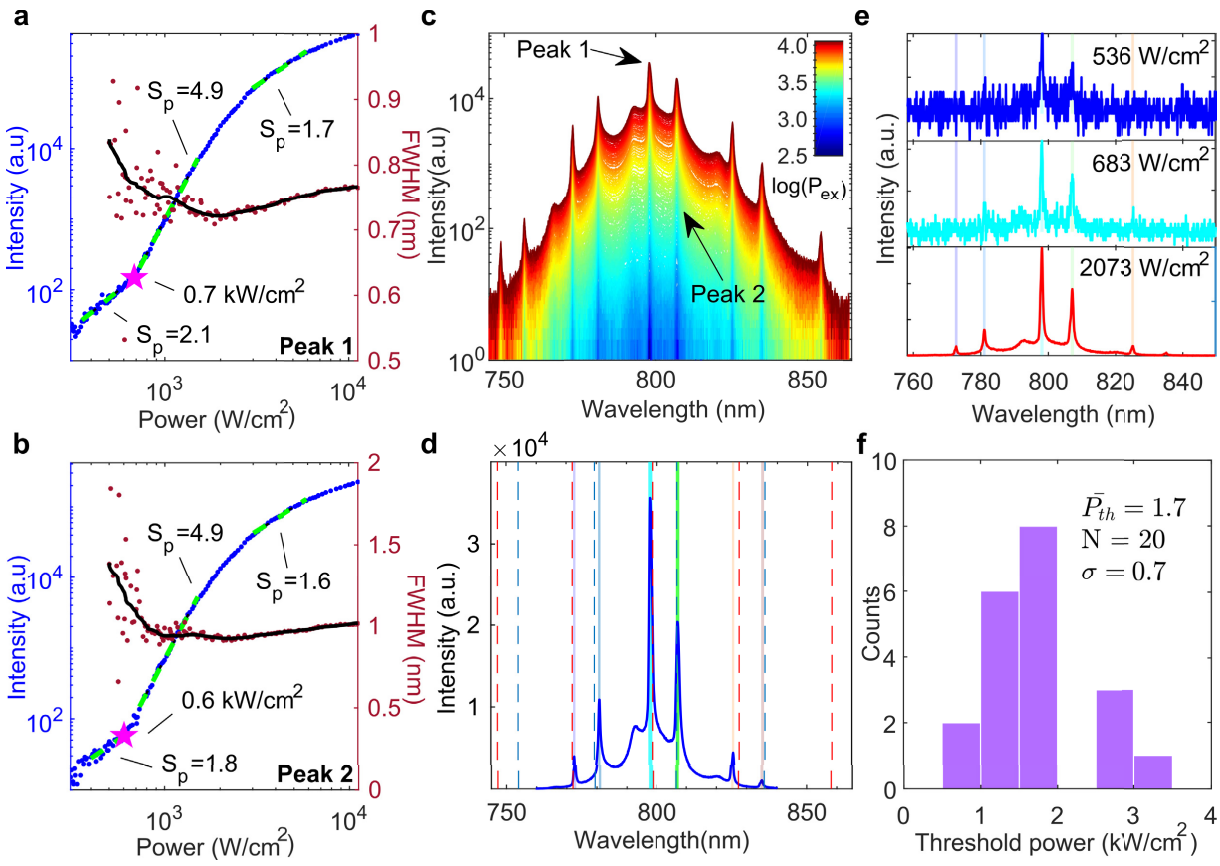

Figure 4. Characterization of upconverted lasing for 5 µm ELNP-PS microsphere resonators. (a-b) Power dependence curves for the two main WGM peaks centered at 798 and 807 nm, labeled as Peak 1 and 2. Emission intensity (I_{em}, blue) and spectral line width (Lorentzian FWHM, red) are plotted as function of 1064 nm pump power density. The smoothed FWHM trace (black) is shown as a guide to the eye. Power law fits (green lines) and their slopes (S_p) are shown for three regions of the curves (pre-lasing, lasing and saturation). The lasing threshold is marked with a magenta star. (c) Emission spectra as function of increasing pumping power on a log scale. (d) Comparison of the measured microsphere emission spectrum (solid blue curve) with the calculated WGM resonance asymptotic solutions $\lambda_{r,m,l}(R, n_{cavity}, n_r, r, m)$ for both the TE (red dashed line) and TM modes (light blue dashed line). Here, R = 2.48 µm, n_{cavity} = 1.586, and r = 1). Green rectangles around the main peaks indicate the bounds used for I_{em} integration. (e) Emission spectrum for pump powers (below, near and above the threshold, corresponding to 540, 680, and 2070 W/cm^2, respectively). (f) Histogram of the lasing thresholds for 20 randomly selected microspheres (only aggregated beads were excluded).

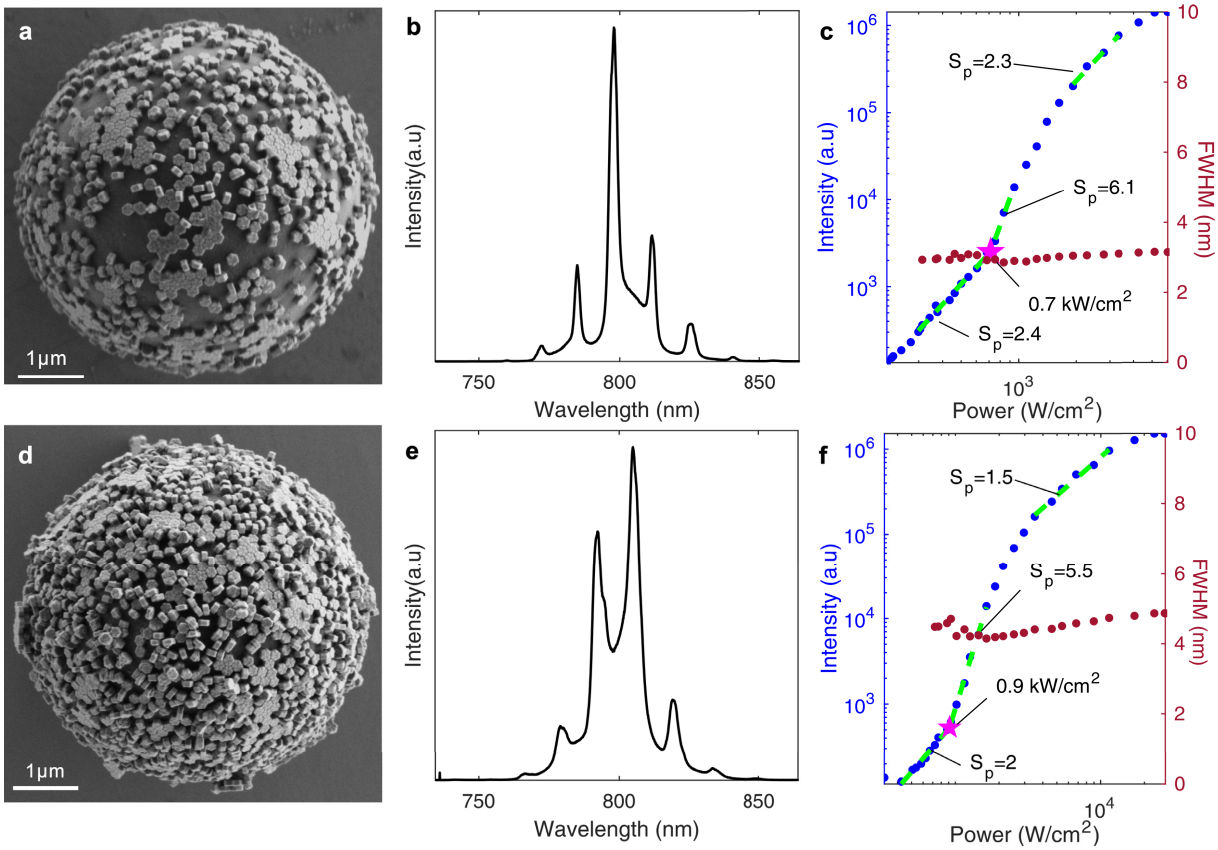

Figure 5. Large β-$NaY_{0.99}Tm_{0.1}F_4$ hexagonal nanoplates (250 × 120 nm) assembled on the surface of a 5 μm polystyrene microcavity. (a, d) Representative SEM micrographs showing hexagonal ELNP nanoplates assembled on the surface of PS microspheres using 0.05 (a) and 0.2 g/mL (d) ELNP/hexane solutions during the fabrication process. Representative emission spectra (b, e) and power dependence curves (c, f) for the main WGM peaks centered at 798 nm (b) and 805 nm (e) for microlasers processed from the same batches as (a) and (d), respectively. Emission intensities (I_{em}, blue) and spectral linewidths (Lorentzian FWHM, red) are shown as function of 1064 nm pump power density. Power law fits (green lines) and their slopes (S_p) are shown for three regions of the curves (pre-lasing, lasing and saturation). Lasing thresholds are marked with magenta stars.

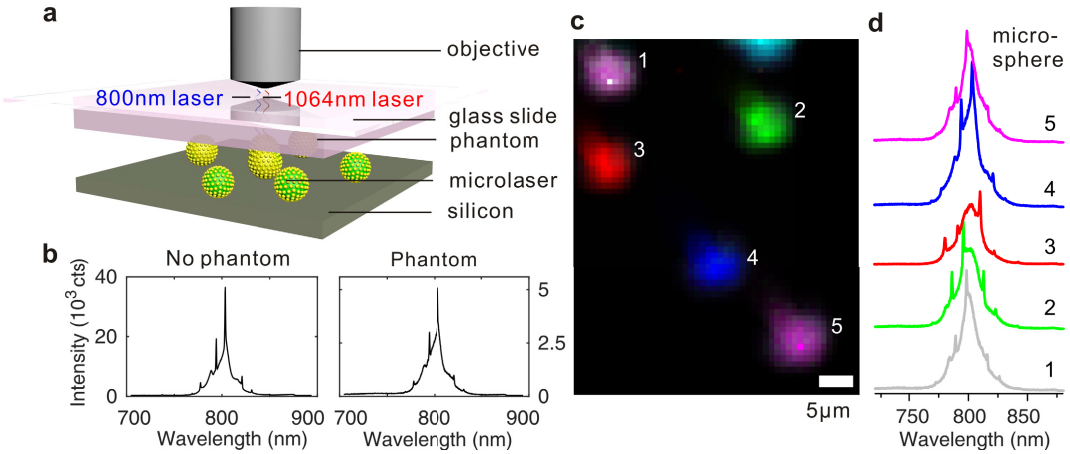

Figure 6. Imaging microlasers through scattering media. (a) Instrumental setup. 1064 nm light is focused by an objective (1700 kW/cm^2) and excites microlasers through a phantom made from 1% agarose and 0.25% intralipid. The 800 nm emission is collected through the phantom by the same objective. (b) WGM spectrum from a single microlaser with (right) and without (left) the presence of a 1 mm thick phantom. Microlasers are 5 μm in diameter and coated with a submonolayer of 15.8 nm core/shell ELNPs, as in Figure 2d. (c) Confocal scanning micrograph of five microspheres imaged through the same phantom as (b). The colors at each point are determined by a least-squares fit of a linear combination of the average spectra of each bead. The colors of each component are those of the numbered traces in Figure 6d. (d) WGM spectra collected at representative positions on the five numbered microspheres shown in (c).

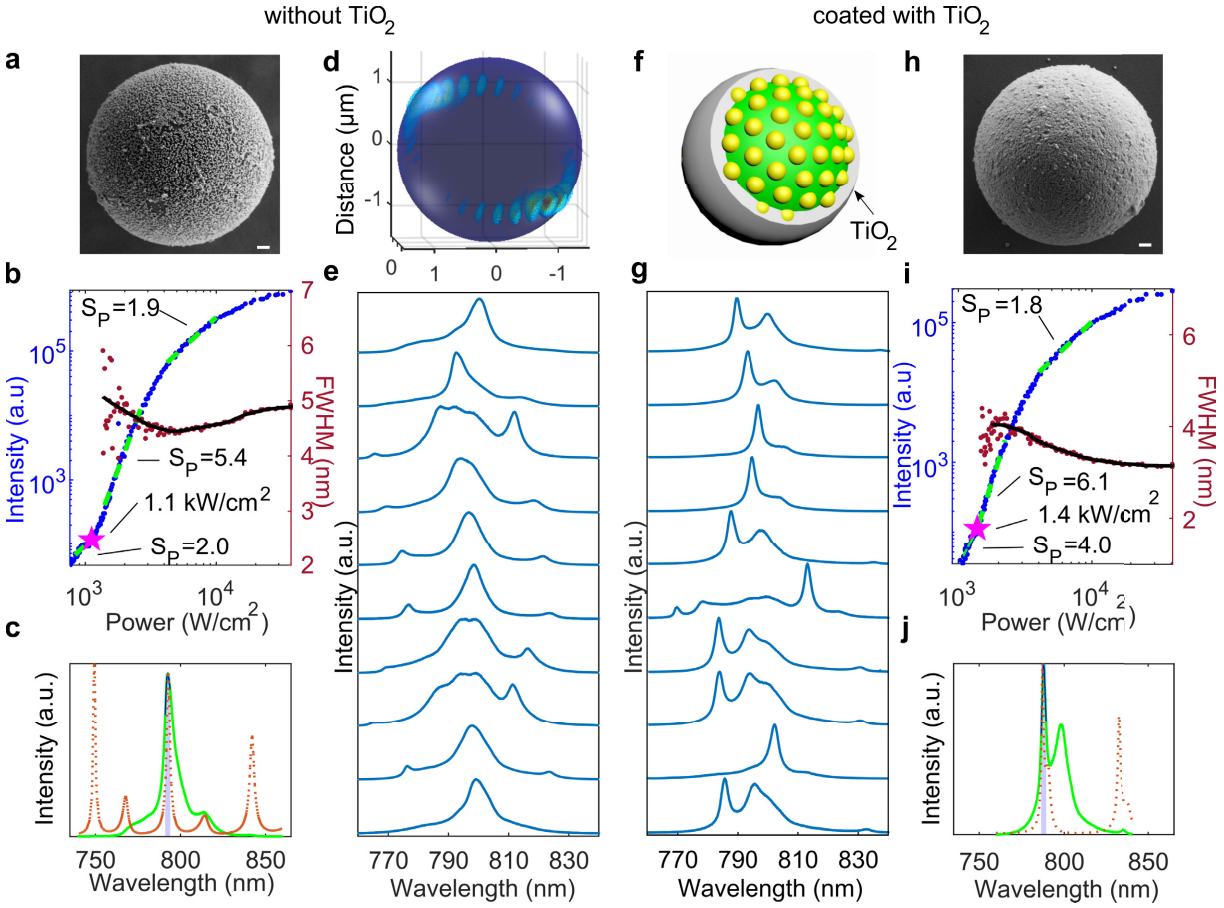

Figure 7. Characterization of upconverted lasing for 3 µm ELNP-PS microsphere resonators without (a-e) and with 20 nm TiO_2 overcoating (f-j). (a, h) SEM micrographs of an uncoated (a) and TiO_2-coated microresonator (h). The scale bar is 200 nm. (b, i) Power dependence curves for the main WGM peak, centered at 793 nm without TiO_2 coating (b) and shifted to 788 nm with TiO_2 coating (i). Emission intensity (blue) and the linewidth (red) are plotted as function of 1064 nm pump power density. Black line is the smoothed FWHM trace. Power law fits (green lines) and slopes (S_p) are shown for pre-lasing, lasing and saturation regions, with the lasing threshold marked with a magenta star. (c, j) Comparison of the measured microsphere emission spectra (green curve) without (c) and with TiO_2 overcoating (j). The simulated WGM resonance FDTD solutions are shown for both TE and TM modes (dashed orange) for bead radii of 1.495 (c) and 1.500 µm (j), with the latter overcoated with a 20 nm layer of TiO_2 (j). Refractive indices n_{cavity} of 1.586 and n_{TiO_2} of 2.4 were used for the calculations without (c) and with (j) TiO_2 overcoating. (d) 3D representation of the transverse electric mode field distribution $|E|^2$. The transverse electric WGM at 793 nm was numerically simulated for a 3 µm ELNP-PS microsphere. (e, g) The emission spectra of 10 different 3 µm ELNP-PS microresonators, without (e) and with (g) TiO_2 overcoating. (f) A schematic representation of the TiO_2 ALD coating on an ELNP-PS microresonator.

Table of Contents Graphic